Applied Energy 261 (2020) 114377

Contents lists available at ScienceDirect

Applied Energy

journal homepage: www.elsevier.com/locate/apenergy

Theoretical performance characteristics of a travelling-wave phase-change thermoacoustic engine for low-grade heat recovery

Rui Yang, Avishai Meir, Guy Z. Ramon*

Department of Civil & Environmental Engineering, Technion – Israel Institute of Technology, Haifa 32000, Israel

HIGHLIGHTS

- The performance of a travelling-wave engine with phase change is analyzed.
- Efficiency > 40% of Carnot limit can be achieved with temperature differences < 50 K.
- The required mean pressure for low-temperature operation is reduced to several bars.
- Criteria for choosing the reactive component are proposed.

ARTICLE INFO

Keywords:
Thermoacoustic engine
Phase change
Wet thermoacoustics
Low-grade heat
Waste heat

ABSTRACT

There is a critical need for environmentally benign, cost-effective technologies to utilize the vast amount of untapped low-grade heat sources. In this work, we report a novel travelling-wave thermoacoustic engine, which incorporates phase change of a condensable component into the classical thermoacoustic conversion, and thus can work efficiently at a low-temperature difference (< 50 K). A numerical model was experimentally validated, based on which a thorough analysis of the engine's onset and steady state under different working conditions was performed. It was found that the presence of phase change can significantly enhance thermoacoustic conversion, leading to increased efficiency and energy density. The presented engine exhibits a thermal-to-acoustic efficiency > 40% of the Carnot efficiency when working at a temperature difference < 50 K. Moreover, the addition of phase change reduces the required mean pressure in the thermoacoustic engine by at least one order of magnitude, which is significant in terms of increasing safety and reducing cost of practical devices.

1. Introduction

Globally, significant amounts of low-grade thermal energy remain untapped; for example, waste heat from exhaust gas, steam and water, account for 72% of the primary energy consumption in the world [1]. In the industrial sector, only 37% of waste heat sources are above 413 K, while almost 30% are within 313–333 K [1]. Meanwhile, the large quantity of low-grade heat available through geothermal wells is not properly used either. In Europe alone, for example, the potential of geothermal energy at 338–393 K is about 150,000 MW [2]. Moreover, ocean thermal energy provides a practically infinite amount of heat, but with the maximum temperature difference being only 20–24 K [3]. Finally, temperatures of 80–120°C are readily accessible through simple solar-thermal collectors, routinely used for heating water at the household level. A major reason for the under-exploitation of low-grade heat is the lack of cost-effective methods. Currently, very few commercially-available technologies can make use of low-grade heat. One leading technique is the organic Rankine cycle (ORC) for electricity generation, which can reach 30–40% of the Carnot efficiency at a temperature difference above 80 K. However, the ORC system often suffers from environmental and safety hazards due to its organic working fluid [4]. Some Stirling engines can reach a similar efficiency when the temperature difference is around 100 K, but the problems of sealing and high cost have so-far prevented large-scale application [5]. Utilizing the Seebeck effect, semiconductor-based solid-state thermoelectric devices can convert low-grade heat directly into electricity, but materials limitations result in low efficiency and costly scale-up [6]. Recently, the thermo-osmotic energy conversion technology [7] and some novel thermo-electrochemical devices, including the thermal capacitive electrochemical cycle [8,9] using supercapacitors [10], the thermally regenerative battery [11] and the direct thermal charging cell [12] have emerged. These devices typically reach an efficiency around

* Corresponding author.
E-mail address: ramong@technion.ac.il (G.Z. Ramon).

https://doi.org/10.1016/j.apenergy.2019.114377
Received 22 September 2019; Received in revised form 5 December 2019; Accepted 14 December 2019

Nomenclature

A	area, m^2
a	sound speed, m/s
c	acoustic compliance per unit length, m^2/Pa
C	molar concentration of reactive component
c_p	isobaric heat capacity, J/kg·K
E	acoustic power, W
F	spatial average function
g	acoustic power source or sink term
$\dot{H}$	total heat flux, W
k	thermal conductivity, W/m·K
l	length, m; acoustic inertance per unit length, kg/m^5
l_h	latent heat, J/mol
M	transfer matrix
$\dot{m}$	molar mass flux, mol/s
p	pressure, Pa
Pr	Prandtl number
Q_h	heating power, W
r	acoustic resistance per unit length, $Pa·s/m^4$
R_g	universal gas constant, J/mol·K
r_h	hydraulic radius, m
Sc	Schmidt number
T	temperature, K
U	volumetric velocity, m^3/s
v	velocity, m/s
x	location, m

Greek letters

α	thermal diffusivity, m^2/s
β	thermal expansion coefficient, K^{-1}
γ	specific heat ratio
η	efficiency; a parameter describing sorption kinetics
ν	kinematic viscous, m^2/s
ξ	porosity
ρ	density, kg/m^3
τ	Womersley number
φ	phase angle, °
ψ	a parameter describing the 'power' of reactive component
ω	angular frequency, rad/s

Special symbols

i	imaginary unit of a complex number
||	absolute value of a complex number
~	complex conjugation
Re	real part of a complex number
Im	imaginary part of a complex number

Subscripts

1	first order, complex amplitude
2	second order
2nd	2nd-law; second
b	boiling
c	cold end
dry	classical thermoacoustic conversion
gas	gas
h	hot end
ideal	ideal case
ld	load
m	mean value
onset	onset of oscillation
s	solid
sys	system
ta	thermal-to-acoustic
wet	phase-change thermoacoustic conversion

Abbreviations

AHX	ambient heat exchanger
HHX	hot heat exchanger
REG	regenerator
TBT	thermal buffer tube

10%-20% of Carnot efficiency in lab-scale experiments, but their application prospects remain unclear as further research is required. Hence, there is an urgent need to develop other clean, efficient and low-cost technologies for low-grade heat recovery.

A thermoacoustic engine converts heat into acoustic power. It possesses several advantageous features, e.g., robustness and high reliability, while also being environmentally benign. Based on characteristics of the acoustic field, thermoacoustic engines may be classified into three forms: standing-wave, travelling-wave, and cascade engine which combines the former two. The travelling-wave engine has the highest efficiency, comparable to that of an internal combustion engine [13], owing to its inherently reversible thermodynamic cycle, which is analogous to an Ericsson cycle. However, to drive the traditional thermoacoustic engine generally requires high-grade heat sources (above 873 K). In the last decade, the low-temperature difference thermoacoustic engine, which typically consists of a looped travelling-wave resonator and one or more locally enlarged thermoacoustic cores, each including a regenerator sandwiched by two heat exchangers, has attracted the interests of many researchers. Although this type of engine can start to oscillate at a temperature difference as low as 20 K, a much higher temperature difference (100–200 K) is required for steady-state operation [14,15]. Furthermore, compared with other commercially-available technologies, the afore-mentioned thermoacoustic engine has lower thermal efficiency and power density. These disadvantages prevent it from large-scale industrial application.

The classical thermoacoustic conversion process can be enhanced by coating the solid surface with a condensed vapor layer, from and onto which evaporation and condensation occur. Raspet et al. firstly verified the enhancement of phase change on thermoacoustic conversion in a standing-wave thermoacoustic demonstrator, in which the onset temperature difference was reduced to 80 K with a wet stack, compared to 280 K with a dry stack [16]. Similar phenomena were also observed in other standing-wave and travelling-wave engines by Tsuda and Ueda [17,18], Noda and Ueda [19] and Kawaminami et al. [20]. Meir et al. reported the steady-state operation of a standing-wave engine working in both ‘dry’ (i.e. classical thermoacoustic conversion) and ‘wet’ (i.e. with phase-change) modes [21]. Atmospheric air was used as the ‘non-reactive’ gas, and the wet mode was realized by soaking the stack in water prior to the experiments. The wet engine operated at a temperature difference 150–200 K lower than its dry equivalent while producing up to eight times more acoustic power [21]. To understand the mechanism of phase-change thermoacoustics, some theoretical work has also been carried out. Based on Rott’s classical theory of thermoacoustics, Raspet et al. developed equations to describe the propagation of sound in the thermoacoustic process with condensation and evaporation [16]. They modified the classical linear thermoacoustic theory by adding the effects of phase change and diffusion to the bulk flow of the working fluid mixture in the continuity equation, as well as the equations describing the transport of heat and mass, and produced work [22]. They also carried out an idealized calculation on a

wet-wall standing-wave thermoacoustic refrigerator, which indicates that both the cooling power and coefficient of performance of the refrigerator can be improved by incorporating phase change in the classical thermoacoustic conversion [22]. Weltsch et al. proposed an approximate model to describe the mass transfer in a quarter-wavelength standing-wave resonator where the humid air undergoes a reversible sorption process [23]. By introducing parameters describing the sorption kinetics and decouple the Clausius–Clapeyron relation from the continuity equation, Offner et al. proposed a more general theory, which is able to describe the thermoacoustic conversion incorporated with any kind of mass exchange process between working fluid and solid surface, including condensation/evaporation but also extendable to reversible reactions such as absorption or adsorption [24]. Yasui and Izu developed a Lagrangian method to investigate the pV work of a fluid parcel moving in the wet stack with in both standing-wave and travelling-wave fields, showing that the thermoacoustic conversion is always enhanced by phase change in the travelling wave field, while it is sometimes suppressed in the standing-wave field [25]. The above-mentioned theoretical body of work has laid the foundation of phase-change thermoacoustic conversion; however, a full analysis of the performance characteristics of a phase-change, looped-travelling wave system has yet to be done.

Up until now, most of the studies on phase-change thermoacoustic engines were focused on the standing-wave engine, which, while shown to be better than the dry mode, is still expected to be less efficient than the travelling-wave engine, due to its intrinsically irreversible thermodynamic cycle. The extent to which the travelling-wave thermoacoustic conversion can be enhanced by the phase change of a condensable species has yet to be studied. In the present study, we report a looped travelling-wave thermoacoustic engine with a binary gas mixture, including a non-reactive gas and a reactive, phase-changing, component, which is shown to significantly enhance thermoacoustic conversion. A thorough numerical investigation of the onset process and steady-state of the engine was carried out. Our results illustrate that this engine exhibits a low onset temperature difference, high acoustic intensity and high efficiency while driven by a low-grade heat source.

2. Model formulation

2.1. Model system

Fig. 1 shows the configuration of a travelling-wave thermoacoustic engine with phase change. It consists of four identical stages, each containing an ambient heat exchanger (AHX), a regenerator (REG), a hot heat exchanger (HHX), a thermal buffer tube (TBT) and a second ambient heat exchanger (2nd AHX). We chose this configuration because it has already been proven to be an efficient classical thermoacoustic engine by de Blok [14], Yang et al. [15], Jin et al. [26,27] and Bi et al. [28]. The dimensions of the main parts are listed in Table 1.

Fig. 1 also depicts a schematic illustration of the thermodynamic cycle executed by the travelling-wave thermoacoustic conversion in the wet mode. The variations of volume, pressure, and temperature of a representative mixture parcel are similar to those of a gas parcel in the dry mode [29], but in the former they are accompanied with phase change and variations in the concentration of the reactive component. Following an idealized, 4-step cycle, beginning with (1), the mixture parcel moves to the left with almost constant pressure, and absorbs heat from the solid surface. Some reactive component evaporates from the liquid film on the solid surface and goes into the parcel due to the increased saturation vapor pressure caused by the temperature rise. In (2), the parcel expands isothermally, accompanied by heat absorption, and the addition of the reactive component, because the partial pressure of the vapor drops. In (3) and (4), which are the reverses of (1) and (2) respectively, the condensations of the reactive component occur because of the temperature drop and pressure rise, respectively. During this cycle, the acoustic power is generated by the expansion of the parcel in (1) and (2), which can be significantly increased by phase changes of the reactive component. Additionally, a mass flux occurs because of the cycle — for a given mixture parcel, the position where condensation occurs is always colder than the place where evaporation occurs. In order to maintain the conservation of reactive component mass, the liquid reactive component has to be drawn back from the cold side to the hot side by some passive force, such as the capillary force of the regenerator, or gravity.

2.2. Governing equations

The working fluid in a phase-change thermoacoustic system is a binary mixture, containing an non-reactive gas and a reactive, condensable component accompanying traditional thermoacoustic conversion with phase change. Under the 'long-wavelength approximation', the flow and heat transfer of the binary mixture in the system can be described by the following equations [24]

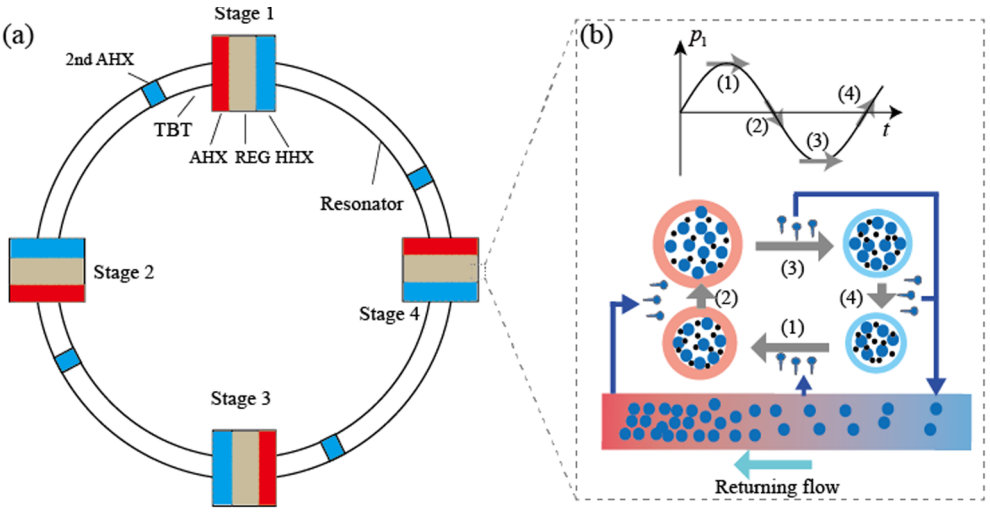

Fig. 1. (a) Schematic of the looped travelling-wave thermoacoustic engine with phase change. It consists of four identical stages, each containing an ambient heat exchanger (AHX), a regenerator (REG), a hot heat exchanger (HHX), a thermal buffer tube (TBT) and a second ambient heat exchanger (2nd AHX). (b) The conceptualized thermodynamic cycle of the travelling-wave thermoacoustic conversion with phase change. The non-reactive and reactive molecules are represented by black and blue dots, respectively. The four thermodynamic steps are similar to those of a gas parcel in the dry mode, but accompanied by phase change and corresponding variations in the concentration of the reactive component: (1) isobaric heat absorption with mass gain, (2) isothermal expansion with mass gain, (3) isobaric heat rejection with mass loss and (4) isothermal compression with mass loss.

Table 1
Dimensions of the main parts of the engine. HHX-hot heat exchanger, REG-regenerator, AHX-ambient heat exchanger, TBT-thermal buffer tube, 2nd AHX-second ambient heat exchanger. ζ-porosity, r_h-hydraulic radius, h-heat transfer coefficient, $\tau_\nu = r_h\sqrt{\omega/\nu}$.

Items	Diameter (mm)	Length (mm)	Details
HHX	97	30	Parallel-plates heat exchanger, ζ is 0.28, r_h is 0.3 mm. h is assumed to be infinite.
REG	97	30	Parallel-plates regenerator, ζ is 0.72, r_h varies to satisfy specific τ_ν.
AHX	97	30	Parallel-plates heat exchanger, ζ is 0.28, r_h is 0.5 mm. h is assumed to be infinite.
TBT	26	100	–
2nd AHX	26	20	Parallel-plates heat exchanger, ζ is 0.8, r_h is 0.5 mm. h is assumed to be infinite.
Resonator	72	790	–

$$\frac{dp_1}{dx} = -\frac{i\omega\rho_m}{F_\nu A_{gas}}U_1, \tag{1}$$

$$\frac{dU_1}{dx} = -\frac{i\omega A_{gas}}{\rho_m a^2}\left[\gamma + F_\alpha(1-\gamma) + \gamma\frac{C_m}{1-C_m}\frac{1-F_D}{\eta_D}\right]p_1 + \left[\frac{F_\nu - F_\alpha}{(1-Pr)F_\nu}\beta + \frac{\frac{\eta_\nu}{\eta_D}(1-F_D)-(1-F_\nu)}{F_\nu(1-Sc)}\frac{C_m}{1-C_m}\frac{l_h}{R_g T_m^2}\right]\frac{dT_m}{dx}U_1, \tag{2}$$

$$\frac{dT_m}{dx} = \frac{\dot{H}_2 - \frac{1}{2}\mathrm{Re}\left[p_1\widetilde{U}_1\left(1-\frac{\widetilde{F}_\nu - F_\alpha}{(1+Pr)\widetilde{F}_\nu}\right)\right] - \dot{m}l_h}{\frac{\rho_m c_p |U_1|^2}{2A_{gas}\omega(1-Pr)|F_\nu|^2}\mathrm{Im}\left[\frac{(\widetilde{F}_\nu - F_\alpha)[1+(1-F_\nu)/(1-F_\alpha)]}{(1+Pr)} - \widetilde{F}_\nu\right] - (A_{gas}k + A_s k_s)}, \tag{3}$$

which are derived from the conservation equations for momentum, mass and energy, respectively. Note that Eqs. (1) and (2) are the dimensional forms of the momentum and mass equations in Ref. [24]. Here, p_1, U_1 and $\dot{H}_2$ represent the complex pressure amplitude, volumetric velocity amplitude and the total energy flux, respectively, while T_m, ρ_m, a, k, γ, c_p and R_g are the mean temperature, density, sound velocity, thermal conductivity, specific heat ratio, isobaric heat capacity and the universal gas constant, respectively. We also define the Schmidt number $Sc = \nu/D$ and Prandtl number $Pr = \nu/\alpha$, where ν, D and α are the kinematic viscosity, diffusion coefficient and thermal diffusivity. A_{gas} and A_s are the cross-sectional areas of the gas channel and the solid respectively, k_s is the thermal conductivity of the solid, ω is the angular frequency and l_h denotes the latent heat of phase change of the reactive component. The functions η_ν and η_D are related to sorption kinetics [23,24] and, for the simple evaporation/condensation considered herein, equal unity. The functions F_n (n = α, ν, or D) are spatial averages arising from the velocity, pressure, temperature and concentration fields; for the parallel-plates geometry of the regenerator assumed in this study, these can be expressed as

$$F_n = 1 - \frac{\tanh[(1+i)\tau_n/\sqrt{2}]}{(1+i)\tau_n/\sqrt{2}}, \tag{4}$$

where $i = \sqrt{-1}$, τ_n is defined as $r_h\sqrt{\omega/n}$ where r_h is the hydraulic radius. The specific expressions of F_n for other segments can also be found in Ref. [30].

C_m is the mean molar concentration of the reactive component, which can be obtained from the Clausius–Clapeyron relation

$$C_m = \exp\left[-\frac{l_h}{R_g}\left(\frac{1}{T_m} - \frac{1}{T_b}\right)\right], \tag{5}$$

where T_b is the boiling temperature of the reactive component. When T_m equals T_b, C_m reaches the limiting value of one. Eqs. (1)–(3) degenerate into their dry forms if C_m is zero. Finally, the longitudinal, time-averaged mass flux of the reactive component, $\dot{m}$, can be written as [23,24]

$$\dot{m} = \frac{1}{1-C_m}\frac{C_m}{2R_g T_m}\mathrm{Re}\left[\widetilde{p}_1 U_1\frac{F_D - \widetilde{F}_\nu}{(1+Sc)\widetilde{F}_\nu}\right] - \frac{1}{1-C_m}\frac{|U_1|^2}{2A_{gas}\omega|F_\nu|^2}\frac{p_m C_m l_h}{R_g^2 T_m^3}\frac{1}{1-Sc^2}\mathrm{Im}\left[\widetilde{F}_\nu(1+Sc) + \frac{\eta_\nu}{\eta_D}(F_D - \widetilde{F}_\nu)\right]\frac{dT_m}{dx} - \frac{p_m A_{gas} D}{1-C_m}\frac{C_m l_h}{R_g^2 T_m^3}\frac{dT_m}{dx}. \tag{6}$$

2.3. Numerical solution methodology

The stability limit, i.e., the critical state of the system, beyond which onset of self-sustained oscillations occurs, is calculated numerically by the transfer matrix method [31]. Specifically, the pressure and volumetric velocity at any point x along the system, can be expressed as the functions of those at (x–Δx)

$$\begin{pmatrix} p_1(x) \\ U_1(x) \end{pmatrix} = M(x, x-\Delta x)\begin{pmatrix} p_1(x-\Delta x) \\ U_1(x-\Delta x) \end{pmatrix}, \tag{7}$$

where M represents the transfer matrix. By applying Eqs. (1) and (2), the transfer matrices for each component can be obtained as

$$\begin{pmatrix} p_1(0) \\ U_1(0) \end{pmatrix} = M_{sys}\begin{pmatrix} p_1(l_{sys}) \\ U_1(l_{sys}) \end{pmatrix}, \tag{8}$$

where M_{sys} is the product of transfer matrices of all components. It is clear that, in the case of a looped system, $x = 0$ and $x = l_{sys}$ in fact refer to the same position, and p_1 and U_1 at $x = 0$ or $x = l_{sys}$ must be nonzero when the system reaches the critical state of onset. In order to have a nonzero solution, M_{sys} must equal the unit matrix, based on which the temperature and frequency at the onset of oscillations can be calculated.

The onset of the oscillations produces a transient state, which could turn into a steady state if equilibria in thermodynamics and acoustics can be achieved asymptotically. In the steady state, we assume that the total heat flux $\dot{H}_2$ is constant in all system segments except in heat exchangers, through which heat is absorbed or rejected. We also assume that there are no temperature gradients, i.e. dT_m/dx is zero, in the resonator and heat exchanger. Next, integrations of the three coupled equations, i.e., Eqs. (1)–(3), in each segment, are performed along the x direction using the fourth-order Runge-Kutta method. Because of the looped configuration, p_1, U_1 and T_m at the start of calculation should be equal to those at the end of calculation, which are used as boundary conditions. By targeting the boundary conditions, the distributions of p_1, U_1 and T_m in the system can then be calculated, and all the other key parameters (ω, C_m, acoustic power, etc.) are then obtained.

In the engine, the regenerator is the only region where thermoacoustic conversion occurs, with all the other system segments consuming acoustic power. Hence, we define the thermal-to-acoustic efficiency as

$$\eta_{ta} = \Delta E_{REG}/Q_h \tag{9}$$

where ΔE_{REG} is the acoustic power difference between the two ends of the regenerator. The corresponding 2nd-law efficiency is

$$\eta_{ta,2nd} = \eta_{ta} T_h/(T_h - T_c), \tag{10}$$

where T_h and T_c are the temperatures of the working fluid at the hot and cold ends of the regenerator, respectively. When extra loads are installed, we define the thermal efficiency as

$$\eta_{ld} = E_{ld}/Q_h, \tag{11}$$

where E_{ld} is the acoustic power dissipated in the load. The corresponding 2nd-law efficiency is then

$$\eta_{ld,2nd} = \eta_{ld} T_h/(T_h - T_c). \tag{12}$$

3. Experimental setup

The mathematical model described in Section 2.2 is generally applicable for the simulation of all loop-structured thermoacoustic devices in which phase change takes place. To verify this model, an experimental looped single-stage thermoacoustic engine was constructed, as shown in Fig. 2, consisting of a regenerator sandwiched by two heat exchangers, a compliance tube and several resonator segments. The regenerator used here is a 600 CPSI ceramic honeycomb with a length of 30 mm and diameter of 94 mm. The hot heat exchanger is made from a 0.2 mm-thick stainless steel sheet and rolled to create corrugated channels with a maximum height of about 2 mm. The input heating is supplied by eight cartridge heaters, embedded within the heat exchanger structure. The ambient heat exchanger is similar to the hot one, but made from a 0.2 mm-thick copper sheet. The heat is removed by water circulated from a chiller. The resonator is a stainless steel tube with an inner diameter of 26 mm. The compliance tube, whose mechanism can be found in Ref. [26], is used to adjust the acoustic field. It is made of stainless steel, with a length of 100 mm and a volume of 0.8 L. The total loop length is around 4 m. The non-reactive gas used is atmospheric N_2, while the reactive component is water, supplied by soaking the regenerator into distilled water for 10 minutes before the experiments.

Two type-K thermocouples were installed at the two ends of the regenerator. Five pressure sensors (GE UNIK 5000 series) were installed along the loop to monitor the pressure wave. The signals from the thermocouples and pressure sensors were acquired by NI 9212 and 9239 analog input modules, respectively. The temperature and the pressure were measured every 5 s, and the data were displayed and recorded by a LabVIEW-based VI.

4. Results and discussion

4.1. Idealized analysis of the thermodynamic cycle

To better understand the phase-change thermoacoustic conversion, motivated by Swift [29], a simple acoustic-electric analog is derived, as follows (see Fig. 3 for a schematic of the circuit analogy). Rearranging Eqs. (1) and (2), we have

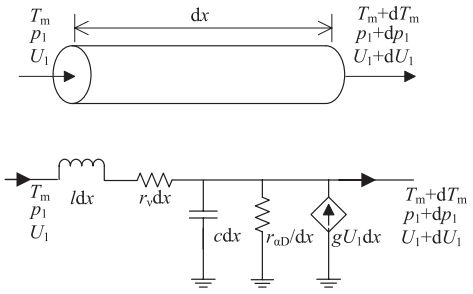

Fig. 3. The acoustic-electric analog of a short tube. L-acoustic inertance, r_ν-viscous resistance, c-acoustic compliance, $r_{\alpha D}$-thermal-diffusive-relaxation resistance, g-acoustic source/sink.

$$\frac{dp_1}{dx} = -(i\omega l + r_\nu)U_1, \tag{13}$$

$$\frac{dU_1}{dx} = -\left(i\omega c + \frac{1}{r_{\alpha D}}\right)p_1 + gU_1, \tag{14}$$

enabling an analogy between the acoustic system and an AC electric circuit. The viscous resistance r_ν and acoustic inertance l can be expressed as

$$r_\nu = \frac{\omega\rho_m}{A}\frac{\mathrm{Im}[F_\nu]}{|F_\nu|^2}, \tag{15}$$

$$l = \frac{\rho_m}{A}\frac{1 - \mathrm{Re}[F_\nu - 1]}{|F_\nu|^2}. \tag{16}$$

The acoustic compliance c, thermal-diffusive-relaxation conductance $1/r_{\alpha D}$ (or thermal-diffusive-relaxation resistance $r_{\alpha D}$) and source (for engine) /sink (for refrigerator) term g can be written as

$$c = \frac{A_{gas}}{p_m\gamma}\left\{1 + (\gamma - 1)Re[1 - F_\alpha] + \gamma Re\left[\frac{C_m}{1 - C_m}\frac{1 - F_D}{\eta_D}\right]\right\}, \tag{17}$$

$$\frac{1}{r_{\alpha D}} = \frac{\omega A_{gas}}{p_m\gamma}\left\{(\gamma - 1)\,\mathrm{Im}[F_\alpha] + \gamma\,\mathrm{Im}\left[-\frac{C_m}{1 - C_m}\frac{1 - F_D}{\eta_D}\right]\right\}, \tag{18}$$

$$g = \left[\frac{F_\nu - F_\alpha}{(1 - Pr)F_\nu}\frac{1}{T_m} + \frac{\frac{\eta_\nu}{\eta_D}(1 - F_D) + F_\nu - 1}{F_\nu(1 - Sc)}\frac{C_m}{1 - C_m}\frac{l_h}{R_g T_m^2}\right]\frac{dT_m}{dx}. \tag{19}$$

Accordingly, the axial variation of the time-average acoustic power can be expressed as [29]

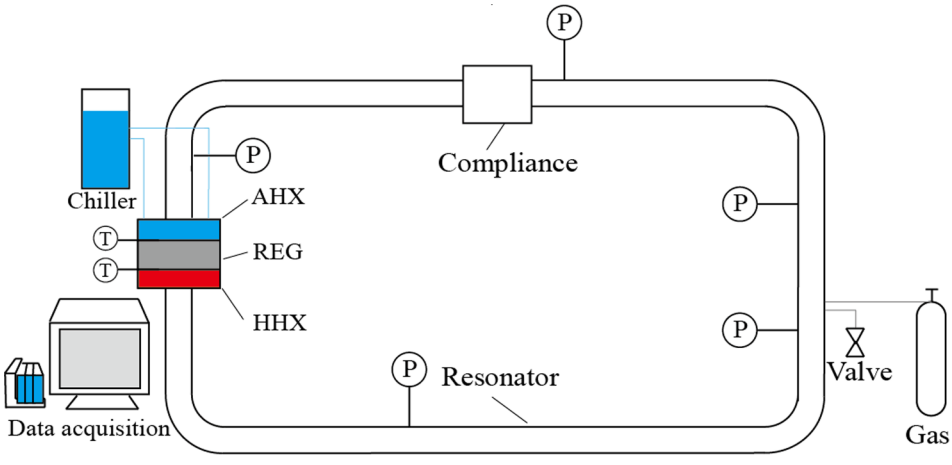

Fig. 2. Experimental setup of the looped single-stage thermoacoustic engine. The regenerator (REG) is a 30 mm-long ceramic honeycomb with a diameter of 94 mm. The hot heat exchanger (HHX) is a 0.2 mm-thick stainless steel sheet rolled to create corrugated channels with a maximum height of about 2 mm. The input heat is supplied by eight cartridge heaters, embedded within the heat exchanger structure. The ambient heat exchanger (AHX) is similar to the hot one, but made from a 0.2 mm-thick copper sheet. The heat is removed by water circulated from a chiller. The compliance tube is used to adjust the acoustic field. The symbols 'T' and 'P' represent thermocouples and pressure sensors respectively.

$$\frac{dE_2}{dx} = -\frac{r_\nu}{2}|U_1|^2 - \frac{1}{2r_{\alpha D}}|p_1|^2 + \frac{1}{2}\mathrm{Re}[g\tilde{p}_1 U_1]. \tag{20}$$

Next, we consider an ideal short regenerator with zero viscosity and perfect thermal contact between the fluid and the solid material [29], and set $F_\nu = 1$, $F_\alpha = F_D = 0$ and $Pr = Sc = 0$. According to Eq. (20), the amplified acoustic power becomes

$$\Delta E_2 = \left[\frac{1}{T_c} + \frac{C_m}{1-C_m}\frac{l_h}{R_g T_c^2}\right](T_h - T_c)E_{2,c}, \tag{21}$$

where $E_{2,c}$ is the acoustic power at the cold end. Therefore, the acoustic power at the hot end is

$$E_{2,h} = \left[\frac{T_h}{T_c} + \frac{C_m}{1-C_m}\frac{l_h}{R_g T_c^2}(T_h - T_c)\right]E_{2,c}. \tag{22}$$

Neglecting heat conduction through the regenerator, the total heat flux is [24]

$$\dot{H}_2 = \dot{m} l_h. \tag{23}$$

Further, neglecting the diffusive losses in Eq.(6), we have

$$\dot{m} = \frac{-C_m}{1-C_m}\frac{1}{R_g T_c}E_{2,c}. \tag{24}$$

Since the input heat is given as

$$Q_h = W_h - \dot{H}_2 = \left[\frac{1}{T_c} + \frac{C_m}{1-C_m}\frac{l_h}{R_g T_c^2}\right]T_h E_{2,c}, \tag{25}$$

the thermal efficiency of an ideal short regenerator is found to be

$$\eta_{ideal} = \frac{\Delta E_2}{Q_h} = \frac{T_h - T_c}{T_c}, \tag{26}$$

showing that the idealized efficiency of the phase-change thermoacoustic conversion equals the Carnot efficiency.

4.2. Model validation

Experimental data from the assembled thermoacoustic engine were compared with the calculated results. As shown in Fig. 4a and b, the model is able to qualitatively describe the basic features of the pressure wave form and the trend of $|p_1|$ with varying Q_h. The calculated values of $|p_1|$ are higher than the experimental data, while the deviations between calculated and experimental values of ΔT are very small (see Fig. 4c). A main reason for the deviations between model and experiment might be that part of the channels within the AHX (and possibly also the regenerator) were blocked by condensed water during the experiments, leading to the decrease of the measured $|p_1|$. Another reason is the assumption of reversible sorption process, which does not account for losses during the phase change. Finally, nonlinear losses due to the abrupt expansion and contraction of the cross section between the regenerator and the resonator also result in calculation error. Since there is only one experimental point of onset in our experiments, the experimental onset temperatures of a single-stage looped thermoacoustic engine from Tsuda and Ueda [17] were used to compare with the corresponding calculated results. As shown in Fig. 4d, the calculated

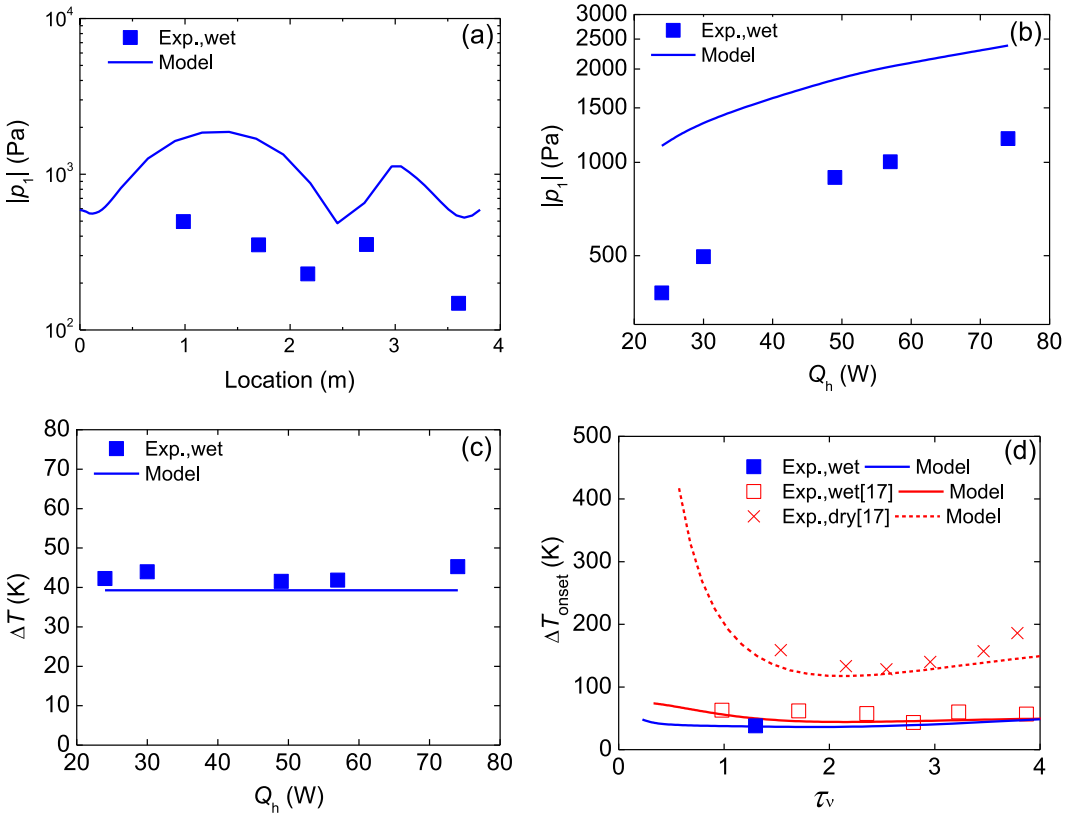

Fig. 4. Comparisons between calculated and experimental results. (a) Pressure amplitude distribution under steady state. (b) Pressure amplitude vs. input heat under steady state. (c) Temperature difference across the regenerator vs. input heat under steady state. (d) Onset temperature difference vs. Womersley number ($\tau_\nu = r_h\sqrt{\omega/\nu}$). The blue squares and lines represent measurements made in our engine and model calculations, respectively, in which p_m is 1 bar, and the mixture is water/N_2. Meanwhile, the red squares are wet-mode results of Ref. [17] with a slightly different system, in which p_m is 1 bar, and the mixture is water/air; the solid red line is the corresponding model calculation. Finally, the red crosses and dashed line are the experimental results in the dry mode from Ref. [17], and corresponding model calculation, respectively, in which p_m is 1 bar, and the working fluid is air. The onset temperatures in the wet mode are much lower than those of the dry mode, because of the enhancement by the phase change.

ΔT_{onset} shows good agreement with the experimental data in both trend and magnitudes. The deviations appear to mainly come from the uncertainties of ± 5 K in the cold-side temperature in the experiments, as well as the uncertainties in the porosities of regenerators in Ref. [17] (assumed to be 0.8 in our calculation).

4.3. Onset analysis

The scaled frequency τ_ν, also known as the Womersley number, is a key parameter for onset in both dry and wet thermoacoustic conversions [23,32]. We compared the onset temperature difference ΔT_{onset} of the wet and dry modes with different τ_ν. At a given τ_ν, ΔT_{onset} in the wet mode is much smaller than that in the dry mode, indicating an enhancement of thermoacoustic conversion due to phase change. It is also observed that there is a minimal ΔT_{onset} at $\tau_\nu = 0.8$ for both modes. In the dry mode, at different τ_ν there is a changing tradeoff between the thermal gain and viscous losses, embodied in the source term g_{dry} [29,32],

$$g_{dry} = \frac{F_\nu - F_\alpha}{(1 - Pr)F_\nu}\beta\frac{dT_m}{dx}. \tag{27}$$

According to Eqs. (4) and (27), there exists an optimal τ_ν for which g_{dry} contributes the most to the acoustic power gain, and accordingly leads to the lowest ΔT_{onset}. In the wet mode, according to Eq. (19), a similar tradeoff that also includes mass transfer contributions exists. Since the value of α is close to D in our calculation, we have

$$g \approx \frac{F_\nu - F_\alpha}{(1 - Pr)F_\nu}\left(\beta + \frac{C_m}{1 - C_m}\frac{l_h}{R_g T_m^2}\right)\frac{dT_m}{dx}, \tag{28}$$

showing that g_{dry} and g share the same dependence on τ_ν, which explains why the optimal τ_ν in the two modes (i.e., wet and dry) are close to each other.

Fig. 5a shows the relation between ΔT_{onset} and $C_{m,h}$, the latter of which is the vapor concentration at the hot end of the regenerator. ΔT_{onset} decreases with the rise of $C_{m,h}$, because the source term g is dramatically amplified, as seen in Eq. (19). Fig. 5a also reveals that the benefit of a high p_m (say, 10 bar or 20 bar) is not obvious in the wet mode, although it is critical and even necessary for lowering ΔT_{onset} in the dry mode [27]. On the one hand, when p_m is low, a small ΔT_{onset} can be achieved by increasing $C_{m,h}$. On the other hand, the increase of p_m brings about the rise of T_b, leading to a higher T_h at onset (see Fig. 5c), which will not only result in a larger viscosity, but also limit the applicable heat source.

As discussed above, a high $C_{m,h}$ is helpful to decrease ΔT_{onset}, but leads to a high T_h at onset. At a given $C_{m,h}$ and p_m, T_h is determined by T_b, which is an inherent property of the reactive component. Furthermore, the performance of the engine is significantly affected by other properties of the reactive component (ρ, k, D, l_h, etc.). Hence, other appropriate reactive components are worth exploring. We selected four reactive components candidates, namely water, ethanol, methanol and 2-propanol. Their latent heat and boiling temperature at 1 bar can be found in the Supplemental Material. Fig. 5b and d show the variations of ΔT_{onset} and T_h at onset at different $C_{m,h}$ with different reactive components. At a given $C_{m,h}$, ΔT_{onset} with water as the reactive component is the largest, mainly because water has the highest viscosity at a given $C_{m,h}$ (see the Supplemental Material). ΔT_{onset} of the other three reactive components are very close to each other. Additionally, T_h at onset with water is the highest, followed by 2-propanol, ethanol and methanol, finally methanol whose T_b is the lowest.

4.4. Steady-state analysis

4.4.1. Acoustic field characteristics

Fig. 6 compares the distributions of temperature and acoustic field in the system when the engine runs in the wet and dry modes. For the convenience of comparison, we set T_h at 332 K, T_c at 311 K (see Fig. 6a) and input heat at 400 W in both modes. In order to enable the system to work at such a low temperature difference, the required p_m is 79 bar in the dry mode, whereas p_m is only 1 bar in the wet mode.

A travelling-wave acoustic field is always preferred in both thermoacoustic conversion and acoustic power propagation [13]. Fig. 6b shows the distributions of the phase of pressure amplitude, φ_p, the phase of volumetric velocity amplitude φ_U and their difference φ_{pU} in the two modes. The curves of these three variables of the wet mode are very similar to those of the dry mode, because the symmetric configuration builds a robust acoustic field which is not significantly changed by phase change. The values of φ_{pU} in the engine are from -19° to 25° in the wet mode, and from -19° to 21° in the dry mode, indicating that the travelling-wave component dominates the engine in both modes. Furthermore, a high acoustic impedance in the regenerator is also necessary for decreasing the viscous loss in the regenerator [13]. That is the reason why a locally enlarged regenerator is adopted in a lot of dry-mode travelling-wave engines [14,15]. This technique is also adopted in our wet mode design. Consequently, as shown in Fig. 6c, the mean values of acoustic impedance in the regenerator reach 8 $\rho_m a$ and 9 $\rho_m a$ in the wet and dry modes, respectively.

As shown in Fig. 6d and e, the wet mode has a much lower $|p_1|$ but a much higher $|U_1|$ than the dry mode, due to the small characteristic acoustic impedance $\rho_m a$ caused by the low p_m. In the regenerator, $|p_1|$ falls due to the large resistance, while $|U_1|$ rises because of the thermoacoustic conversion. From Fig. 6f, ΔE_{REG}, the acoustic power generated in the regenerator through thermoacoustic effect, in the wet mode, is almost double that in the dry mode, although the acoustic power flowing in the loop E_2 is much lower than that in the dry mode. Accordingly, the thermal-to-acoustic efficiency η_{ta} in the wet mode also is double that in the dry mode. The main reason behind the superior performance of the wet mode is that the acoustic source term g can be significantly enhanced by the presence of the condensable vapor, according to Eq. (19). Considering that $C_{m,h}$ in the wet case is only 0.2, there is still much room for further improvement by increasing the vapor concentration.

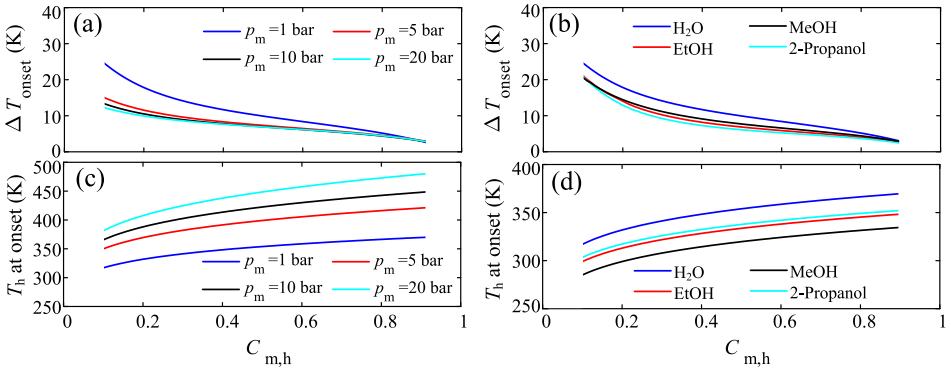

Fig. 5. Onset temperature difference and the corresponding hot end temperature, vs. vapor concentration. In (a) and (c), four mean pressures, i.e., 1, 5, 10 and 20 bar are used, and the working mixture is water/N_2. In (b) and (d), four different reactive components, i.e, water (H_2O), methanol (MeOH), ethanol (EtOH) and 2-propanol are used, while the inert gas is N_2. The mean pressure is $p_m = 1$ bar and the Womersley number ($\tau_\nu = r_h\sqrt{\omega/\nu}$) is fixed at 0.8 in all subfigures.

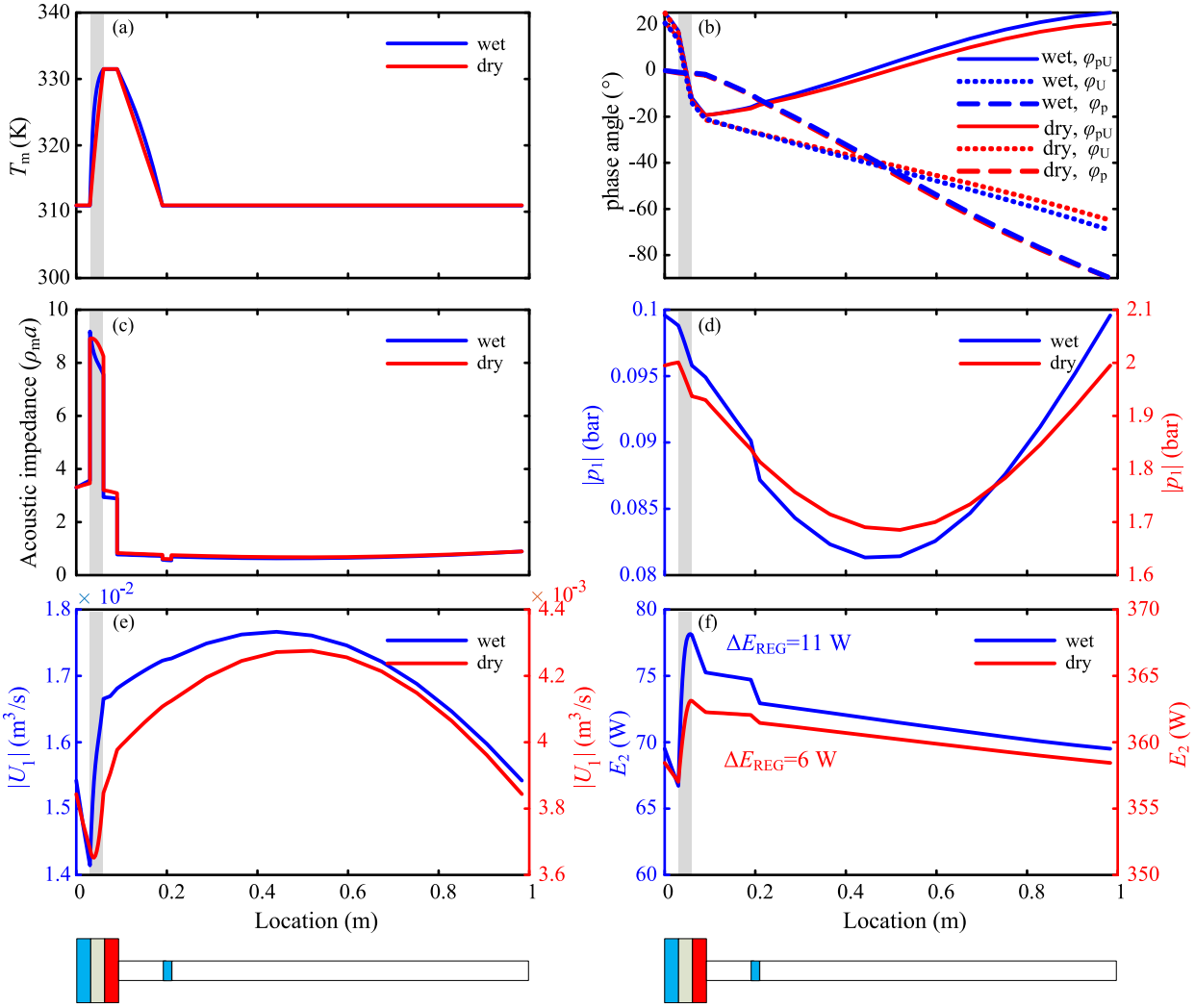

Fig. 6. Distributions of temperature and the acoustic field along the repeating unit in the loop, shown for the wet and dry modes. (a) Temperature. (b) Phase angle. (c) Acoustic impedance. (d) Pressure amplitude $|p_1|$. (e) Volumetric velocity amplitude $|U_1|$. (f) Time-average acoustic power E_2. The gray-shaded region represents the regenerator, where the thermoacoustic conversion occurs. The working fluid is N_2 in the dry mode, and N_2/water mixture in the wet mode. The geometric dimensions of the engine in the two modes are identical (see Table 1) except the values of the hydraulic radius of the regenerator, which is modified as necessary to keep a fixed value of $\tau_\nu = 0.6$ in both modes. The temperature difference and input heat are 21 K and 400 W in both modes. In order to enable the engine to function at such a small temperature difference, p_m is 79 bar in the dry mode, but is only 1 bar in the wet mode.

4.4.2. Performance of the engine without load

In this section, the influence of Womersley number, mean pressure, vapor concentration and reactive component on the steady-state performance of the engine will be investigated. The input heat will be fixed at 100 W, and the 2nd-law efficiency $\eta_{ta,2nd}$ will be used as a main indicator to evaluate the performance of the engine, because the temperature difference changes dramatically with the variation of $C_{m,h}$. Fig. 7 shows the change of $\eta_{ta,2nd}$ with different τ_ν. An optimal τ_ν with which $\eta_{ta,2nd}$ is maximized exists in each curve, because of the interplay between thermal, diffusive and viscous effects. The optimal τ_ν is around 0.6, regardless of changes in p_m and $C_{m,h}$. Hence, τ_ν will be set fixed at 0.6 in the following discussion.

The properties of the reactive component also have a profound influence on steady-state performance. Four factors should be taken into consideration for choosing an appropriate reactive component. The first factor is the boiling temperature, T_b, which determines the operating temperature range of the engine. The second one is the parameter ψ [24],

$$\psi = \frac{C_m}{1 - C_m} \frac{l_h}{R_g T_m}, \tag{29}$$

which represents the 'power' of the reactive component because there is a positive correlation between ψ and the acoustic source term g according to Eq. (19). For all reactive components, ψ increases with the temperature, particularly near the boiling temperature. The third is the viscosity, which is one of the main sources of acoustic power loss [13], hence, a low viscosity is always favored. The last factor is the interplays between viscous and thermal effects, and between viscous and diffusive effects according to Eq. (19). Given that the change of ν is always accompanied by the variations of α and D, two dimensionless numbers, namely Pr and Sc, should be considered. Generally, a small Pr is always preferred [33], as well as a small Sc.

The values of T_b, ν, Pr and Sc with various C_m of the reactive components used in this study at 1 bar can be found in the Supplemental Material. In the current study, ν and Sc have a profound influence on the performance of the engine, while Pr has a less significant impact. This is because when $C_m < 0.4$, the four reactive components examined here, have similar values of Pr. When $C_m > 0.4$, $\psi \sim 10$, indicating that the diffusive term overweighs the thermal term in Eq. (12). Consequently, the influence of Pr on the source term g is much smaller than that of Sc.

Fig. 8a presents the variation of η_{ta} with different $C_{m,h}$ of different

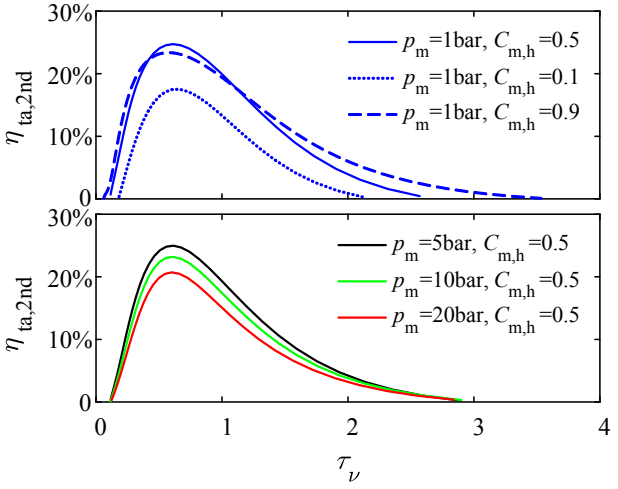

Fig. 7. Calculated 2nd-law efficiency of thermal-to-acoustic conversion vs. Womersley number ($\tau_\nu = r_h\sqrt{\omega/\nu}$) in the wet mode. Top panel – different vapor concentrations at a constant mean pressure. Bottom panel – different mean pressures at constant concentration. The highest $\eta_{ta,2nd}$ appears at a Womersley number ~0.6, regardless of the variation of vapor concentration and mean pressure. The working mixture is water/N_2.

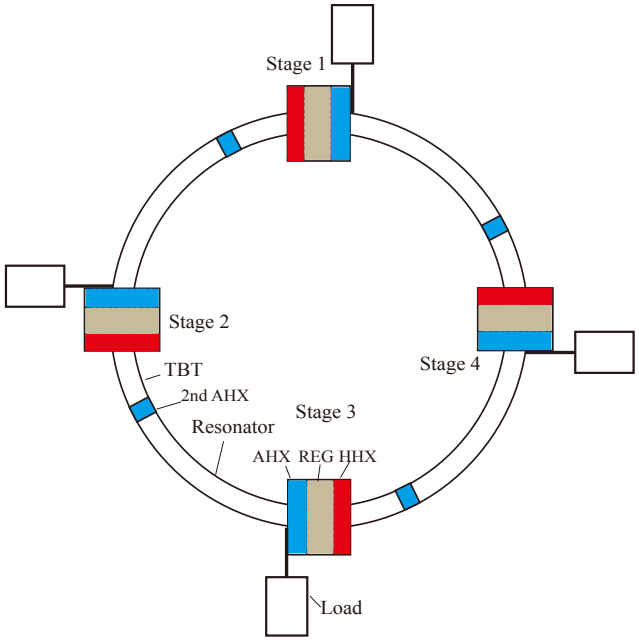

Fig. 9. Schematic of the travelling-wave thermoacoustic engine with a load. HHX-hot heat exchanger, REG-regenerator, AHX-ambient heat exchanger. The load can be any device consuming acoustic power, e.g., a linear alternator, a pulse tube cryocooler, etc.

reactive components, showing that η_{ta} decreases with the increasing $C_{m,h}$, because of the decreasing ΔT (see Fig. 8d), which reduces the corresponding Carnot limit. According to Eqs. (3) and (6), at a given heat flux, a smaller temperature difference is required if C_m is increased, since the longitudinal mass flux $\dot{m}$ is increased. That is the reason why ΔT drops.

Fig. 8c presents the value of $\eta_{ta,2nd}$ with various $C_{m,h}$ of different reactive components. When $C_{m,h}$ is small, the mixture containing methanol (MeOH) as the reactive component has the highest $\eta_{ta,2nd}$, because of its relatively low ν and *Sc*. The result for water is also quite good, because of its low *Sc*. However, as $C_{m,h}$ keeps rising, the performance of the mixture with water becomes the worst, due to the increased ν and *Sc*. The mixture with 2-propanol has the lowest *Sc* and ν when $C_{m,h}$ is high, so its $\eta_{ta,2nd}$ is the highest, which can reach 55% when $C_{m,h}$ is 0.7.

4.4.3. Output performance of the engine with loads

In order to test the output performance of the system, an acoustic load, which can be a linear alternator, is added to each stage at the joint between the AHX and the resonator, as shown in Fig. 9. In this example, we use a heat source at 340 K to drive the engine, and methanol is employed as the reactive component since its mixture with nitrogen exhibited the highest $\eta_{ta,2nd}$ at this temperature (see Fig. 8c). We use 5 bar mean pressure, in order to reduce the viscous loss in the resonator, heat exchangers and thermal buffer tube. The acoustic impedance of the load is set fixed at $(9 + 9i) \times 10^6$ kg/(s·m^4), which is a result of a rough optimization procedure.

Fig. 10 presents the performance of the engine with the load. The solid lines represent the data of the engine with the regenerator dimensions shown in Table 1, while the dashed lines show results with a different regenerator whose porosity and length are 0.9 and 20 mm, respectively. Both E_{ld} and ΔT increase steadily with Q_h, and we note that ΔT rises rather slowly—about 1 K/kW. This might be counter-intuitive to some reaseachers experienced in traditional thermoacoustic engine. The reason behind the slow growth of ΔT is that, the presence of phase change enable the engine to carry much more heat flux than its dry equivalent at a given temperature gradient, according to Eq. (3). The maximal 2nd-law efficiency $\eta_{ld,\ 2nd}$ is 38%, and the corresponding η_{ld} and E_{ld} are 3.6% and 15 W, respectively. At this operating point, the engine works at a T_h of 340 K and T_c of 308 K. The drop of $\eta_{ld,\ 2nd}$ as Q_h rises is caused by the increasing viscous loss. Assuming that the load is a linear alternator with the same acoustic impedance, a practical estimation of the acoustic-to-electric efficiency is 70% [34], which leads to a maximum 2nd-law thermal-to-electric efficiency of 27%.

Additionally, it should be noted that, for the system decribed here, when $Q_h > 2000$ W, $|p_1|/p_m$ might be greater than 0.1 in some segments of the system, which is beyond the low-amplitude limitation of

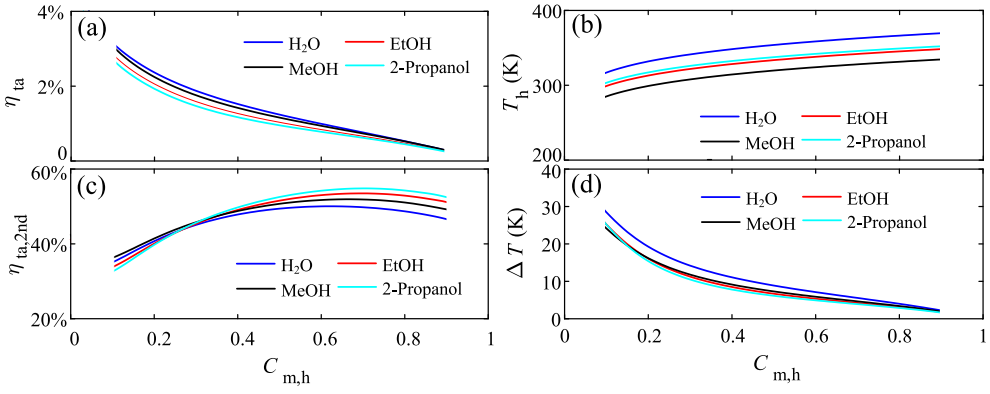

Fig. 8. Calculated performance of the engine using four different reactive components: water (H_2O), methanol (MeOH), ethanol (EtOH) and 2-propanol. N_2 is used as the reactive gas. (a) Thermal-to-acoustic efficiency vs. hot side vapor concentration. (b) Hot side temperature vs. vapor concentration. (c) The corresponding 2nd-law efficiency vs. hot side vapor concentration. (d) Temperature difference along the regenerator vs. hot side vapor concentration. p_m = 1 bar and the Womersley number ($\tau_\nu = r_h\sqrt{\omega/\nu}$) is fixed at 0.6.

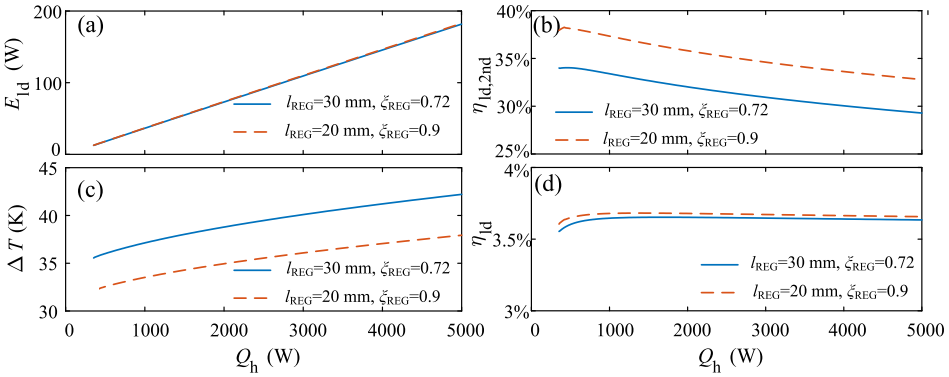

Fig. 10. Performance of the engine with load, capable of extracting power. (a) Output acoustic power vs. input heat. (b) 2nd-law efficiency vs. input heat. (c) Temperature difference along the regenerator vs. input heat. (d) Thermal efficiency vs. input heat. The solid line represents calculations made with l_{REG} (length of regenerator) of 30 mm and ξ_{REG} (porosity of regenerator) of 0.72, while the dashed line represents calculations made with l_{REG} of 20 mm and ξ_{REG} of 0.9. The working mixture is methanol/N_2. p_m = 5 bar.$\tau_\nu = r_h\sqrt{\omega/\nu}$, it is fixed at 0.6. $C_{m,h}$ = 0.26 (T_h = 340 K).

the linear model used here, and may cause significant deviations. That is the reason why we only focus on the utilization of low-grade heat sources. The performance under large temperature difference, which is considered to be very attractive but significantly influenced by non-linear effects, has been scheduled in our near future efforts.

As a final note, our preliminary experiments have highlighted some technical challenges that need to be overcome before the full potential of this novel engine can be realized. First, an appropriate material for the regenerator must be found. To be specific, the regenerator must allow the reactive component to be efficiently transported in the axial direction, without any blockage due to liquid accumulation within the channels. It should also allow the condensed or adsorbed vapor to be continually recycled back to the hot section of the engine, to ensure constant supply. The second one is the high-performance heat exchanger. In our current experimental setup, we used parallel-plates heat exchanger, which works well at low heating power, but for better performance, more efficient heat transfer through phase change or direct contact should be considered.

5. Concluding remarks

In this work, we have studied a looped travelling-wave thermoacoustic engine with phase change. A binary mixture including one non-reactive gas and one reactive component is used, so that evaporation/condensation can occur during thermoacoustic conversion. Following experimental verification, a numerical model was used to assess the characteristics of both onset and steady state of the engine, as affected by various parameters and operating conditions.

According to our analysis, the presence of phase change can not only dramatically reduce the onset temperature difference of the engine, but also significantly enhance thermoacoustic conversion in steady-state operation, leading to increased efficiency and energy density. The presented travelling-wave thermoacoustic engine with phase change is able to work at a temperature difference below 50 K, under which our model predicts that a thermal-to-acoustic efficiency greater than 40% of the Carnot efficiency can be achieved. This temperature difference can be supplied by abundant, low-grade heat sources. Moreover, compared with the traditional thermoacoustic engine, a much lower mean pressure is required, which can result in significantly reduced fabrication costs and increased safety.

A thermoacoustic engine may be used for electricity production or to drive a thermoacoustic heat-pump for cooling applications. Doing so with no environmentally hazardous materials, little to no moving parts and at low temperatures, using accessible and abundant heat sources, would be a major technological development for a more sustainable future.

CRediT authorship contribution statement

Rui Yang: Conceptualization, Methodology, Software, Validation, Investigation, Writing - original draft. **Avishai Meir:** Resources, Data curation, Writing - review & editing. **Guy Z. Ramon:** Conceptualization, Supervision, Writing - review & editing, Project administration, Funding acquisition.

Declaration of Competing Interest

The authors declare that they have no known competing financial interests or personal relationships that could have appeared to influence the work reported in this paper.

Acknowledgements

This research was supported by Grant No. 216-11-024 from the Israel Ministry of Energy and Water. R.Y. was supported, in part, by a fellowship from the Israel Council for Higher Education.

Appendix A. Supplementary material

Supplementary data to this article can be found online at https://doi.org/10.1016/j.apenergy.2019.114377.

References

[1] Forman C, Muritala IK, Pardemann R, Meyer B. Estimating the global waste heat potential. Renew Sustain Energy Rev 2016;57:1568–79.
[2] Vega LA. Ocean thermal energy conversion primer. Mar Technol Soc J 2002;36(4):25–35.
[3] Quoilin S, Van Den Broek M, Declaye S, Dewallef P, Lemort V. Techno-economic survey of organic rankine cycle (ORC) systems. Renew Sustain Energy Rev 2013;22:168–86.
[4] Preißinger M, Schwöbel JAH, Klamt A, Brüggemann D. Multi-criteria evaluation of several million working fluids for waste heat recovery by means of organic rankine cycle in passenger cars and heavy-duty trucks. Appl Energy 2017;206:887–99.
[5] Wang K, Sanders SR, Dubey S, Choo FH, Duan F. Stirling cycle engines for recovering low and moderate temperature heat: a review. Renew Sustain Energy Rev 2016;62:89–108.
[6] Wang C, Li M, Chiu C, Chang T. Kinetic study of solid-state interfacial reactions of p-type (Bi, Sb) 2Te3 thermoelectric materials with Sn and Sn–Ag–Cu solders. J Alloy Compd 2018;767:1133–40.
[7] Straub AP, Yip NY, Lin S, Lee J, Elimelech M. Harvesting low-grade heat energy using thermo-osmotic vapour transport through nanoporous membranes. Nat Energy 2016;1(7):16090.
[8] Atlas I, Ramon GZ. Periodic energy conversion in an electric-double-layer capacitor. J Colloid Interface Sci 2018;530:675–85.
[9] Härtel A, Janssen M, Weingarth D, Presser V, van Roij R. Heat-to-current conversion of low-grade heat from a thermocapacitive cycle by supercapacitors. Energy Environ Sci 2015;8(8):2396–401.
[10] Zhou Y, Huang Y, Pang J, Wang K. Remaining useful life prediction for supercapacitor based on long short-term memory neural network. J Power Sources 2019;440:227149.
[11] Rahimi M, Kim T, Gorski CA, Logan BE. A thermally regenerative ammonia battery with carbon-silver electrodes for converting low-grade waste heat to electricity. J Power Sources 2018;373:95–102.
[12] Wang X, Huang YT, Liu C, Mu K, Li KH, Wang S, et al. Direct thermal charging cell for converting low-grade heat to electricity. Nat Commun 2019;10(1):1–8.
[13] Backhaus S, Swift GW. A thermoacoustic stirling heat engine. Nature 1999;399:335–8.
[14] de Blok K. Multi-stage travelling wave thermoacoustics in practice. Proceedings of

the Nineteenth International Congress on Sound and Vibration 2012.
[15] Yang R, Wang Y, Jin T, Feng Y, Tang K. Development of a three-stage looped thermoacoustic electric generator capable of utilizing heat source below 120 °C. Energy Convers Manage 2018;155:161–8.
[16] Raspet R, Slaton WV, Hickey CJ, Hiller RA. Theory of inert gas-condensing vapor thermoacoustics: propagation equation. J Acoust Soc Am 2002;112(4):1414–22.
[17] Tsuda K, Ueda Y. Critical temperature of traveling-and standing-wave thermoacoustic engines using a wet regenerator. Appl Energy 2017;196:62–7.
[18] Tsuda K, Ueda Y. Abrupt reduction of the critical temperature difference of a thermoacoustic engine by adding water. AIP Adv 2015;5(9):097173.
[19] Noda D, Ueda Y. A thermoacoustic oscillator powered by vaporized water and ethanol. Am J Phys 2013;81(2):124–6.
[20] Kawaminami S, Sakamoto S, Fukuda S, Watanabe Y. Step-type thermoacoustic system saturated with water vapor: study for stabilization of low-temperature driving. Jpn J Appl Phys 2017;56(7S1):07JE12.
[21] Meir A, Offner A, Ramon GZ. Low-temperature energy conversion using a phase-change acoustic heat engine. Appl Energy 2018;231:372–9.
[22] Slaton WV, Raspet R, Hickey CJ, Hiller RA. Theory of inert gas-condensing vapor thermoacoustics: transport equations. J Acoust Soc Am 2002;112(4):1423–30.
[23] Weltsch O, Offner A, Liberzon D, Ramon GZ. Adsorption-mediated mass streaming in a standing acoustic wave. Phys Rev Lett 2017;118(24):244301.
[24] Offner A, Yang R, Felman D, Elkayam N, Agnon Y, Ramon GZ. Acoustic oscillations driven by boundary mass exchange. J Fluid Mech 2019;866:316–49.
[25] Yasui K, Izu N. Effect of evaporation and condensation on a thermoacoustic engine: a Lagrangian simulation approach. J Acoust Soc Am 2017;141(6):4398–407.
[26] Jin T, Yang R, Wang Y, Liu Y, Feng Y. Phase adjustment analysis and performance of a looped thermoacoustic prime mover with compliance/resistance tube. Appl Energy 2016;183:290–8.
[27] Jin T, Yang R, Wang Y, Feng Y, Tang K. Low temperature difference thermoacoustic prime mover with asymmetric multi-stage loop configuration. Sci Rep 2017;7(1):7665.
[28] Bi T, Wu Z, Zhang L, Yu G, Luo E, Dai W. Development of a 5 kW traveling-wave thermoacoustic electric generator. Appl Energy 2017;185:1355–61.
[29] Swift G W. Thermoacoustics: a unifying perspective for some engines and refrigerators. Acoustical Society of America, American Institute of Physics Press, New York, 2002.
[30] Ward B, Clark J, Swift GW. Design environment for low-amplitude thermoacoustic energy conversion, DeltaEC Version 6.2 Users Guide. USA: Los: Alamos National Laboratory; 2008.
[31] Ueda Y, Kato C. Stability analysis of thermally induced spontaneous gas oscillations in straight and looped tubes. J Acoust Soc Am 2008;124(2):851–8.
[32] Yazaki T, Iwata A, Maekawa T, Tominaga A. Traveling wave thermoacoustic engine in a looped tube. Phys Rev Lett 1998;81(15):3128.
[33] Swift GW. Thermoacoustic engines. J Acoust Soc Am 1988;84(4):1145–80.
[34] Timmer MAG, de Blok K, van der Meer TH. Review on the conversion of thermoacoustic power into electricity. J Acoust Soc Am 2018;143(2):841–57.